AIAA JOURNAL
Vol. 45, No. 3, March 2007

Excitation of Instabilities in the Wake of a Wing with Winglets

Sebastian Kauertz* and Günther Neuwerth†
RWTH Aachen University, 52062 Aachen, Germany

DOI: 10.2514/1.26462

This paper describes experimental investigations of possibilities to destabilize the vortex wake behind a wing by using winglets with integrated rudders. These rudders can be deflected statically, as well as oscillated periodically around their static deflection. The oscillation is intended to excite instabilities inherent in the vortex system to provoke an accelerated decay of the vortices. The used model also comprises deflectable ailerons and was equipped with a pair of trailing edge flaps to modify the vortex system. Quantitative wake investigations by particle image velocimetry have been conducted up to 43 spans behind the wing model in a water towing tank. Results show a clear earlier decay of the vortex system and abatement of induced rolling moments in the wake for certain rudder configurations in comparison to the clean wing configuration. However, the oscillation of the winglet rudders did not lead to a further acceleration of vortex decay compared to the statical case in the frame of the experiments conducted.

Nomenclature

A	=	amplitude amplification
b	=	span
b_0	=	vorticity centroid span
C_L	=	lift coefficient
c	=	chord
$c_{L\alpha}$	=	lift slope
$c_{\mathrm{RM,ind}}$	=	induced rolling moment coefficient
$c_{\mathrm{RM,max}}$	=	max. induced rolling moment coefficient in plane
d	=	diameter
f	=	oscillation frequency
k	=	wave number
Re	=	Reynolds number
r_c	=	core radius
t	=	time
t^*	=	normalized vortex age
t_0	=	time for vortex system to descend one centroid span
u_∞	=	freestream velocity
v_z	=	measured vertical velocity
x	=	downstream position
y	=	spanwise position
z	=	vertical position
α	=	angle of attack
Γ	=	circulation
Γ_{WL}	=	circulation of winglet vortex
Γ_0	=	initial circulation
γ	=	growth rate
δ	=	aileron deflection
η, ζ	=	disturbance in y- and z-axis directions
κ	=	amplitude ratio
Λ	=	aspect ratio
λ	=	wavelength
ν	=	winglet dihedral
ρ	=	density
σ	=	standard deviation, eigenvalue
Φ	=	disturbance vector
χ	=	winglet rudder deflection
ω	=	vorticity

Presented as Paper 3470 at the 24th AIAA Applied Aerodynamics Conference, San Francisco, California, 5–8 June 2006; received 11 July 2006; revision received 30 October 2006; accepted for publication 3 November 2006.

*Research Engineer, Institute and Chair of Aerospace Engineering, Wüllnerstrasse 7. Member AIAA.

†Senior Research Engineer, Institute and Chair of Aerospace Engineering, Wüllnerstrasse 7. Member AIAA.

I. Introduction

STRONG vortex wakes of modern transport aircraft are still a considerable hazard where aircraft fly in close staggering such as in the vicinity of airports. The necessary separation between two aircraft during takeoff or landing to minimize this hazard is also a main limiting factor to the capacity of airports. Thus, measures are sought to reduce the hazard posed by these strong vortex wakes to aircraft following closely behind the vortex-generating plane. One approach to this is to use instabilities, which are inherent in a vortex system typically generated by a conventional transport aircraft. When the parameters of the vortex system (circulations, positions, core radii) are within the right range, and these instabilities are excited, they lead to a quick destruction of the vortices. Several experimental investigations have been conducted over the past few years to determine under which conditions an instability develops that can significantly reduce the hazard to a following aircraft. Crouch [1] proposed using oscillating ailerons to enhance the breakdown of a system of trailing vortices. He presented theoretical studies as well as flow visualizations showing the capability of such a system to accelerate the linking of the vortices into vortex rings, but no comprehensive quantitative flow measurements were made yet. The circulation ratio of the additional vortex pairs of a multiple-vortex system was identified as one major factor influencing the linking process. Ortega [2] conducted experiments with a wing model in a towing tank which employed trailing edge flaps of different sizes and positions on a simple wing model to produce a system of two vortex pairs. He showed that with a certain combination of vortex circulation and span ratio between the two pairs, a significantly faster decay of the wake vortex can be achieved. The results were acquired by measurements of the flowfield as well as comprehensive flow visualizations of the evolution of the vortex wake. Stuff [3] and Vollmers [4] similarly investigated passive means to alleviate the wake vortex behind aircraft, supporting the results from former studies. This work was taken up by Haverkamp [5], who could reproduce the significant acceleration of the vortex breakdown in multiple-vortex systems. Similar experimental studies with a generic wing/tail model were done by Durston et al. [6], which again showed a clear influence of tail vortex circulation and span ratio on the decay of the hazard level behind the model, quantified by means of the induced rolling moments on a following wing. The stronger the tail vortices with respect to the wing-tip vortices, and the higher the span ratio between the two pairs, the faster the decay usually takes place. Other research at ONERA [7], for example, comprised investigations on the influence of differential flap settings

on the vortex wake, which can be used to create a multiple-vortex system as well, and the influence of a winglet on the resulting vortex roll up in the near field behind the wing tip. Incorporation of rudders into winglets has been considered by Park and Rokhsaz [8], but detailed experimental results of their influence on the development of the wake vortex in the far field are still missing.

In the work presented here, a simple generic wing model, equipped with outboard ailerons and winglets has been used to investigate how rudders integrated into the winglets can be used to accelerate the initiation of the instabilities. For this purpose the winglet rudders can be deflected statically, as well as oscillated periodically with a variable frequency and amplitude. The vortices forming at the winglet are excited in this way, being moved with the oscillating rudder tip while the model is towed forward. The additional ailerons integrated into the model are used to create another, counter-rotating pair of vortices and thus a vortex system with strong inherent instabilities. The idea follows the proposal of Crouch [1] to use control surfaces on an aircraft wing to actively excite instabilities in the vortex system. These instabilities were originally discovered by Crow [9] for a single pair of counter-rotating vortices, and recently described in more detail by Crouch [10] and Fabre [11,12] for two pairs of vortices. Recent experimental studies by Haverkamp [5] have shown that an active excitation of both vortex pairs by using the ailerons can lead to a significant acceleration of the decay of the vortex wake. In the work presented here, however, only the winglets have been used to excite the tip vortices forming there, after an unstable multiple-vortex system has been created before by using the ailerons and winglet rudders. The intention is to excite the shorter-wavelength instabilities found by Crouch and Fabre et al. as these promise much higher growth rates than the Crow instability. The excitation is limited to the winglet vortices, as they pose the greatest source of hazard in the wake of this model because of their strong circulation. Furthermore, preceding theoretical investigations have shown that a large growth of the perturbation amplitudes can be achieved with this kind of excitation as well. The approach of only one oscillating rudder pair obviously also introduces periodic variation of the lift and induced drag generated by the wing, which makes it impracticable for installation on real aircraft in this arrangement. Thus, the experiments are to be viewed as fundamental investigations only. However, if successful, a compensation of the lift variation by phase-shifted oscillation of other available control surfaces like ailerons is still conceivable.

The theoretically most favorable frequencies for an excitation have been determined by a numerical stability analysis of the emerging vortex systems. The input parameters for this are taken from experiments with statical rudder deflections in different configurations. For each resulting vortex system a calculation is then carried out, which yields the optimal frequency for active excitation. The integrated winglet rudders are then oscillated with this frequency, and the resulting flowfield can be compared to that of the statical reference case. By means of this periodic excitation it is hoped to accelerate the decay of the vortices.

II. Experimental Setup

A. Towing Tank

Experiments have been carried out in the water towing tank of the Institute of Aeronautics and Astronautics at the RWTH Aachen University (see Fig. 1). It has a cross section of 1.5 m width by 1.0 m height and a length of 9 m. This tank allows observation of a fixed plane of the wake after the model has passed it, so that the evolution of the wake up to $x/b = 43$ spans behind the model can be followed. The water-filled tank has a free surface and is otherwise surrounded by glass windows to allow optical access from all directions. To dampen out surface waves produced by towing the model through the tank on its sting, the free surface is covered by two plastic mats, leaving open only a slit for the sting. The towing rig is mechanically decoupled from the test section to prevent transmitting vibrations into the water. The model is towed at a speed of $u_\infty = 1.0$ m/s in all cases, corresponding to a Reynolds number based on wing chord of $Re = 85,000$. Thus the experimental results cannot be transferred to flight conditions directly and should be viewed as basic investigations into the physics involved. The model is accelerated over a distance of about 1.5 m and decelerates over about 0.5 m at the end of the tank. The measurement plane is roughly in the middle between the start and the endpoint of the run. The start and endpoints have been put as close as possible to the face sides of the tank to prevent disturbances generated by starting and stopping the model from reaching the measurement plane for as long as possible.

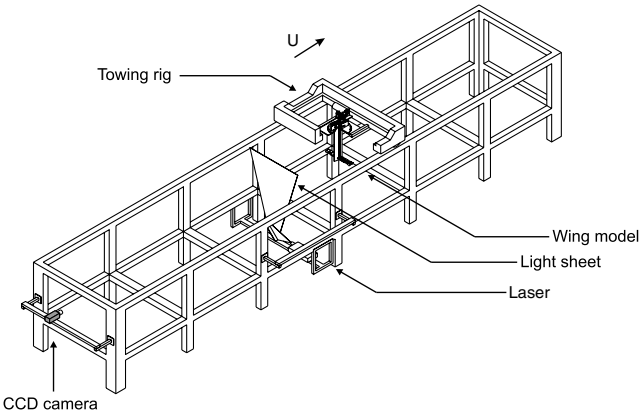

Fig. 1 Water towing tank.

The distance to the vortex-generating wing will be given in wing spans according to $x/b = u_\infty t/b$. Additionally it can expressed in terms of the normalized vortex age t^*. This relates the vortex age to the time the vortex system needs to move one initial vortex spacing downward. It is calculated as

$$t^* = \frac{x}{u_\infty t_0} = \frac{x\Gamma_0}{u_\infty 2\pi b_0^2} \tag{1}$$

according to Gerz et al. [13], with b_0 being the initial spacing of the vortex system and Γ_0 its initial circulation. It is thus dependent upon the actual configuration of the vortex system. The maximum distance in the measurements of $x/b = 43$ here corresponds to a normalized vortex age of, for example, $t^* \approx 0.4$ for the clean configuration at $\alpha = 11$ deg.

B. Model

The model used for the investigations presented here consists of an unswept rectangular wing with swept winglets on the tips (see Fig. 2). The winglets have a dihedral of $\nu = 45$ deg relative to the main wing. Overall aspect ratio including winglets is $\Lambda = 6.9$ with a total span of $b = 0.58$ m. The chord of the main wing is $c_{\text{wing}} = 0.085$ m. The chord of the winglet tip is $c_{\text{winglet}} = 0.050$ m. The profile of the wing section and winglet is a symmetrical NACA0014. The model is attached to the towing rig on a sting consisting of a NACA0022 profile with a chord of $c_{\text{sting}} = 0.1$ m. Model and sting are both manufactured from solid aluminum, only containing the necessary cutouts for the winglet rudder mechanism and thus are very rigid. General dimensions of the model are shown in Fig. 3.

The main wing of the model contains two split ailerons per wing half that can be deflected statically at an arbitrary angle δ. The winglets possess one rudder each being deflectable at angles between $\chi = +20$ deg and -20 deg. A positive angle always denotes a downward deflection. The configurations without any rudder or aileron deflection at both angles of attack are referred to as clean configurations. Additionally, the winglet rudders can be deflected periodically with a variable frequency by a motor. The rotational motion is converted to a translational motion of a linkage running through the sting by an eccentric gear at the top of the sting. That translation is then converted back into a periodic rotation of the shaft driving the winglet rudders which runs through the model up to the winglets. By changing the gear ratio of the excentric gear, different amplitudes of rudder oscillation can be realized.

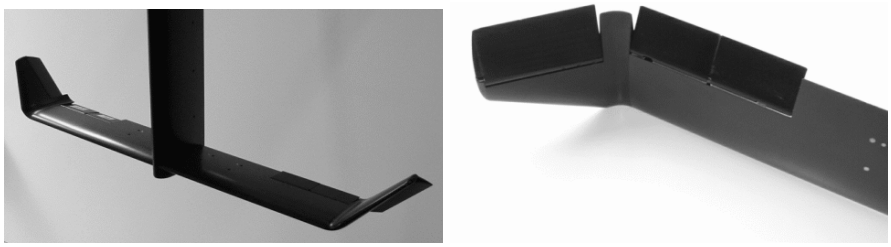

a) b)

Fig. 2 Model with winglets and rudders.

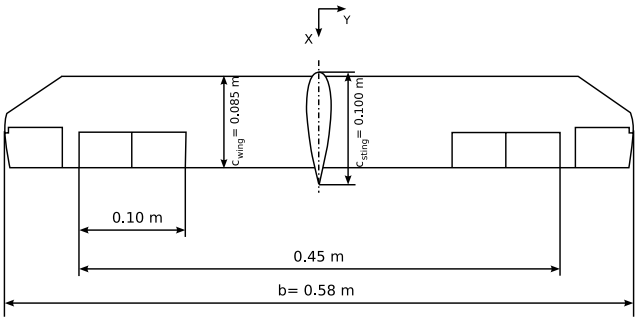

Fig. 3 General dimensions of model.

C. Flow Visualization

The model has also been equipped with thin vinyl tubes to discharge air bubbles into the water for flow visualization. They are introduced close to the tip and at the base of the winglets, so they gather in the core of the vortices forming there. The bubbles are produced by pressurizing a container half filled with water. The air will partly dissolve in the water over a time span on the order of 12 hours at a pressure of $p \geq 6$ bar. When released into the water at about ambient pressure, very small air bubbles will form which follow the flow very well. This method has been described by Neuwerth [14]. If close enough to a vortex, they will concentrate in its core due to the pressure conditions thereby making its trail visible. Proper illumination of the test section allows a visual observation as well as video recording for later evaluation (see Figs. 20 and 21). The behavior of the air bubbles in the core allows a limited evaluation of the properties of the flow. The wavelength of potential sinusoidal perturbations of the vortex trails can be estimated by deriving the length from the known towing speed of the model passing the test section and the time code of the video recording. In this way lengths can be determined to an accuracy of about $\pm 10\%$. However, because of the fixed angle of the camera detailed information about the three-dimensional behavior of the vortices cannot be made. As the core of a decaying vortex enlarges over time, it finally is no longer able to hold many air bubbles in its core. After that happens, the development of the vortices is no longer observable.

D. Particle Image Velocimetry

Two-component particle image velocimetry (2C-PIV) is used as a nonintrusive, optical measuring method. With this method, a plane of the flow is illuminated by a pulsed laser light sheet. The flow is seeded with reflective particles which should ideally follow the flow. These are recorded using a digital charge-coupled device (CCD) camera. The movement of the particles between two laser pulses then allows determination of the velocity of the particles within the light sheet. The material of the particles depends on the flow medium. In the setup used here, polyamide particles with a mean diameter of $d = 55$ μm and a density of $\rho = 1.016$ g/cm^3 have yielded good results. Their diameter and density ensure a good following behavior, while they are large enough to reflect enough light for the camera.

2C-PIV yields only the velocity components in the illuminated plane. Velocity components perpendicular to the plane would require a second camera recording the light sheet at the same time. When the velocity components perpendicular to the plane are in the order of the in-plane components, projection errors due to the image reproduction in the camera lens require a three-component setup to be compensated. As a towing tank is used with an initially resting flow, the out-of-plane components are small compared to the in-plane components. Previous experiments have shown maximum magnitudes of around $v_x = 0.01$ m/s at a towing speed of $u_\infty = 1$ m/s, while the maximum tangential velocities in the plane are around $v_{\theta,\max} = 0.25$ m/s. Furthermore, for determining vorticity and circulation distribution behind the wing, and assessing the vortex hazard to a following wing in the wake, the in-plane velocity components are sufficient. Thus, 2C-PIV is applicable here, which has the further advantage of an easier setup and calibration procedure and less memory consumption of the digital image recordings compared to three-component PIV. For the measurements a 1.4 MPixel SensicamQE CCD camera was used. The observed field, covering the left half-plane of the model, had an extent of 600 mm $\times$ 440 mm. The distance from camera to measurement plane is about 4 m. A Quantel Twins Ultra 120 double-head pulsed Nd:YAG (neodymium-doped yttrium aluminium garnet) laser with a pulse energy of 125 mJ was used to create the light sheet. Camera and laser were operated at a frame rate of 4 Hz, thus recording four velocity distributions of the flow per second. The total measurement time per run of 25 s, corresponding to 100 frames, allows observation of the flow up to $x/b = 43$ spans behind the model.

E. External Influences

Inherent when using a confined test section as in the experiments presented here are the influences on the flowfield in the medium, which have to be taken into account. The presence of the walls causes a deviation of the trajectory of the vortices if they come too close to the walls. Figure 4 shows the trajectory of the winglet tip vortex in the measurement plane for a configuration without rudder or aileron deflections at $\alpha = 11$ deg up to a distance of $x/b = 43$. The model is

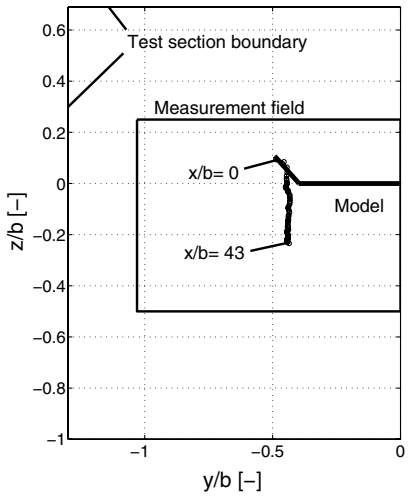

Fig. 4 Trajectory of tip vortex in clean case at $\alpha = 11$ deg up to $x/b = 43$.

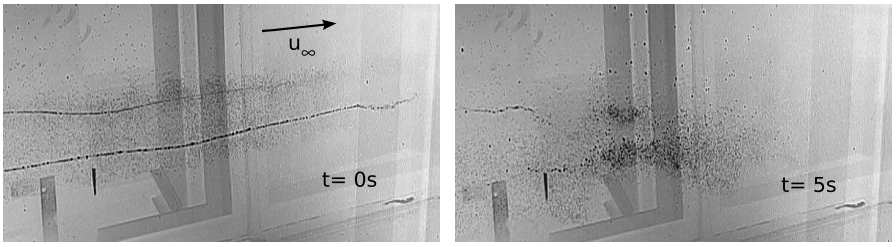

a) $t = 0\ s$ **b)** $t = 5\ s$

Fig. 5 Visualization of end effects at end of test section.

shown in relation to the total extent of the left half-plane of the measurement section. The distance of the wing tip to the side walls is about 0.8 spans, whereas the distance of the model to the bottom is 1 span. It can be seen that no visible lateral deviation occurs in the trajectory, which would indicate an influence of the bottom wall, and the minimum distance of the vortex system to the bottom is still about 0.8 spans. Because the configuration shown is the most stable system at the high angle of attack used, none of the other examined vortex systems descends further than the one shown here. Considering the equally large distance to either side wall of the tank, an influence of these is also unlikely. Furthermore, a possible influence would affect all the investigated configurations in the same way, so differences between configurations must be due to changes in the configurations themselves. It is assumed that the primary influence of wall effects on the wake is negligible.

Another influence examined especially in a towing facility is the end effect produced by the sudden start and stop of the model at the ends of the test section. This in turn produces vortices which end suddenly, imposing a pressure gradient on them and causing a vortex bursting which propagates along the vortices. This effect has been studied in detail, for example, by Bao and Vollmers [15]. Here, a flow visualization of the winglet tip vortex at the end of the towing tank after an experimental run has given an indication as to how fast these disturbances move toward the measurement plane in the given setup (see Fig. 5). Shown here are two recordings separated by 5 s. Within that time, the visible disturbance moves from the right edge upstream by roughly 0.5 m, corresponding to a speed of 0.1 m/s, which is about 40–50% of the maximum tangential velocities observed in the wake. Based upon this estimate, and given an uncertainty in the determination of the propagation speed of about ±10%, it can be expected that the measurement plane, at a distance of about 4 m to the stop point of the model, will be reached by the disturbance not earlier than 36 s after stopping the model. The PIV measurement only runs on for 21 s after the model stopped. Additionally, the significant effects start at around 15 spans distance to the model, corresponding to a measurement time of about 9 s, so it is assumed that other effects are responsible for these, and the disturbance due to the end effect is not dominant in the measurement plane.

Between consecutive measurement runs, a certain time has to pass for the water to become calm. As it would take too long for the water to come to a complete rest, the waiting time (minimum 30 min) has been chosen so that the average velocity in the test section died down sufficiently. The residual velocities then had a magnitude of only about $v_{\theta,\max} = 0.005$ m/s without any preferred direction. Investigations before the measurements have shown that a waiting time of 60 min did not result in noticeably lower residual velocities, which shows that a considerably longer time would be needed for them to become even smaller. However, the results discussed in Sec. VI suggest that these residual velocities do actually have an influence on the evolution of the wake.

F. Evaluation of Experimental Data

To evaluate the hazard the generated wake vortex poses to a following aircraft, the induced rolling moments on a virtual following wing based on the measured velocity distributions have been examined. The induced rolling moment coefficient on a rectangular wing, placed horizontally in the measured plane, has been calculated using a simple stripe method, which results to

$$c_{\mathrm{RM,ind}} = \frac{2}{b_F^2} \int_{-b_F/2}^{b_F/2} c_{L\alpha} \arctan\left(\frac{v_z}{u_\infty}\right) y' \, \mathrm{d}y' \tag{2}$$

with b_F being the span of the following wing and v_z the vertical component of the measured velocity field. The lift slope has been chosen as $c_{L\alpha} = 2\pi$ for simplicity. This coefficient has been calculated for the whole measured plane by moving the following wing over the whole field. A small portion at the left and right edges of the field must be left unprocessed, as there is no velocity data present for one half of the wing (see Fig. 6a). A small following wing span of $b_F = 0.2b$ has been chosen, allowing evaluation of the greatest part of the velocity field. This span ratio corresponds to a typical ratio of an aircraft of Federal Aviation Administration (FAA) category "small" following an aircraft of category "heavy." A typical induced rolling moment distribution is shown in Fig. 6b. The dots mark the centers of the vortices as shown, for example, in Fig. 8a.

From this distribution the maximum coefficient $C_{\mathrm{RM,max}}$ is determined and can be tracked over the whole measurement run up the maximum distance of 43 spans behind the model. In Fig. 7 this progress of the maximum induced rolling moment is shown for a

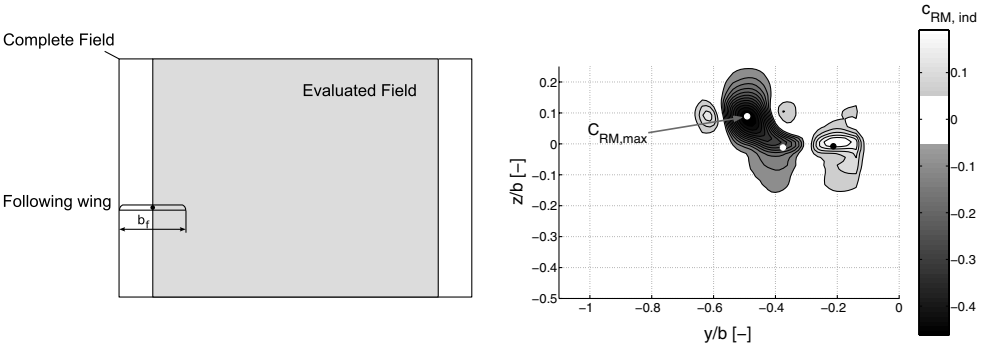

a) Portion of measurement plane available for evaluation.

b) Induced rolling moment coefficient distribution for configuration $\chi = +10$ deg, $\delta = +20$ deg, $\alpha = 11$ deg at $x/b = 0.1$; dots mark vortex centers.

Fig. 6 Evaluation of induced rolling moment coefficients.

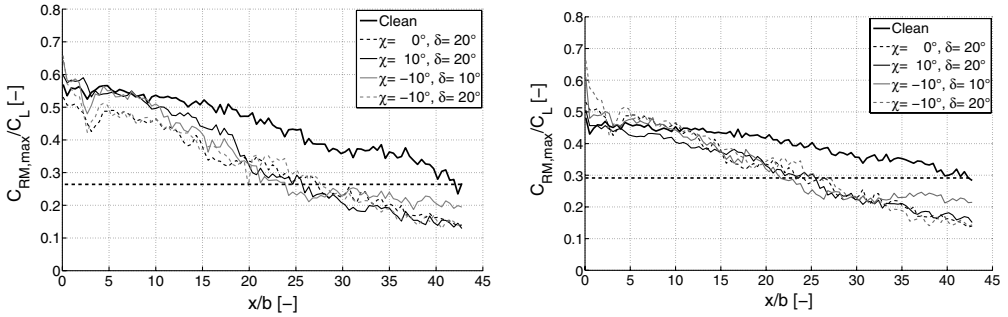

a) $b_F/b = 0.2$ **b)** $b_F/b = 0.3$

Fig. 7 Influence of b_F on the induced rolling moment of various configurations, $\alpha = 11$ deg.

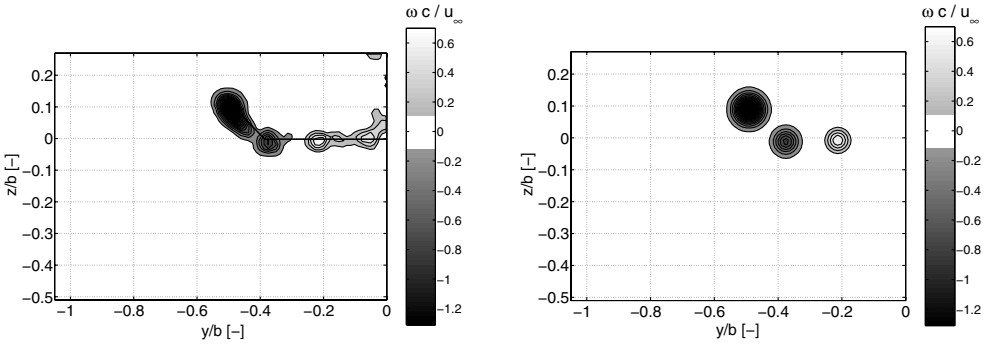

a) Measured vorticity distribution **b) Vorticity distribution from Lamb-Oseen model**

Fig. 8 Comparison of Lamb–Oseen fit with measured vorticity distribution, $\chi = +10$ deg, $\delta = +20$ deg, and $\alpha = 11$ deg.

following wing span of $b_F = 0.2$ as well as $b_F = 0.3$ for comparison. It can be seen that the overall slope of the rolling moment development is slightly less steep for the higher following wing span; however, the qualitative and quantitative conclusions drawn from the results remain the same. In the case shown here an induced rolling moment remains at the end of the measurement which is about 50% lower than for the clean configuration. Also, the final induced rolling moment of the clean configuration is reached already after about 60% of the time by all configurations. These results are discussed in more detail in Sec. IV.

The lift coefficient C_L is calculated by integrating the measured vorticity distributions at the trailing edge along the wing span. For that reason, it can only be determined in the first plane of the measurement. Furthermore, to determine the positions of the vortices as well as parameters like core radius and circulation the measured data are fitted to a Lamb–Oseen vortex model in the first measured plane at $x/b = 0.1$. Figure 8 shows a comparison between measured and fitted vorticity. Each vortex is approximated by a single Lamb–Oseen vortex. The resulting vortex circulation and span ratios and their core radii from the measurements without rudder oscillation are then used as input for the theoretical calculations later on.

III. Theoretical Background

Theoretical description of the vortex system and the evolving instabilities are based upon work done mainly by Crouch [10] and Fabre et al. [11,12]. The vortices generated by the wing are modeled as filaments having a circulation Γ_i (see Fig. 9). They interact with each other through mutual velocity induction according to the law of Biot–Savart. Because symmetry with respect to the centerline of the model is assumed, the vortex positions can be expressed by the span b_i of corresponding vortices of both half-planes. The vortex system is then characterized by the circulation and span ratios of the different vortex pairs, in the case of a 4-vortex system by the ratios Γ_4/Γ_2 and b_2/b_1. The total circulation in one half-plane is then $\Gamma_0 = \Gamma_2 + \Gamma_4$. The distance between the vorticity centroids of each half-plane is b_0 and is used as a reference length for nondimensional quantities.

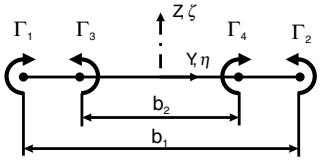

Fig. 9 The 4-vortex system.

The vortex filaments now become superimposed with periodic perturbations of an arbitrary wave number k, which are considered small compared to the spacing of the vortices. The position vector of any point of a vortex filament can then be expressed as

$$\boldsymbol{r}_n = x_n \boldsymbol{i} + (y_n + \eta_n e^{ikx_n})\boldsymbol{j} + (z_n + \zeta_n e^{ikx_n})\boldsymbol{k} \tag{3}$$

From this the perturbation components, which represent the deviation from the unperturbed vortices, can be combined, for example, for a 4-vortex system, as a vector

$$\Phi = (\eta_1, \eta_2, \eta_3, \eta_4, \zeta_1, \zeta_2, \zeta_3, \zeta_4)^T \tag{4}$$

In the case of two vortices per half-plane, a period of the rotation of the vortices around each other can be determined. This periodicity allows a Floquet analysis according to Nayfeh and Mook [16], yielding the eigenmodes of the system and corresponding growth rates γ of possible unstable modes. For a detailed description of the stability analysis refer to Crouch [10] and Fabre [11]. The growth rate is defined as

$$\gamma = \frac{\ell_n(\sigma)}{T} \tag{5}$$

with σ being the eigenvalues of the corresponding eigenmode, and T being the rotation period of the vortices of one half-plane around each other. A system of four vortices with 2 degrees of freedom each has eight eigenmodes, which may or may not be unstable. Instability is indicated by a growth rate $\gamma > 0$.

Depending on rudder settings, the model can also produce a system of six distinct vortices, or three vortex pairs, which interact in

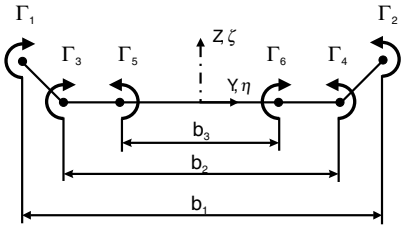

Fig. 10 The 6-vortex system.

the wake of the model. In that case the vorticity at the winglet rolls up into a vortex at the bend between the main wing and the winglet in addition to the vortex at the winglet tip. For such a system an analysis according to Crouch is no longer possible because no rotation period of the vortices around each other can be determined, which is used as a time frame in which stability is investigated. For that reason the evolution of the vortex system is determined directly by integrating the linearized Biot–Savart equations over time, using the same formulation of the equations as in the Floquet analysis. A comparison of the perturbation amplitudes of different cases after a comparable time span then gives an indication of the instability potential of the corresponding configuration. The general structure of such a 6-vortex system is shown in Fig. 10.

The system is characterized by the span ratios b_2/b_1 and b_3/b_1 of the inner vortices to the winglet tip vortex as well as the circulation ratios Γ_4/Γ_2 and Γ_6/Γ_2. Additionally the vertical distances of the vortices to the innermost aileron vortex z_2/z_6 and z_4/z_6 are used to define the positions. The origin of the coordinate system here lies on the connection line between the two innermost vortices.

From the integration over time the magnitude of the perturbation amplitudes after a certain time can be derived. The magnitude relative to the initial perturbation at the wing is a measure for the instability of the system. By calculating this over a range of different wave numbers, one can determine that wave number at which the perturbation amplitudes grow at the fastest rate. For evaluation of the instability potential, a ratio of the perturbation amplitudes of all vortices between the end and the beginning of the integration is determined:

$$A = \frac{\|\Phi(t = t_{\max})\|}{\|\Phi(t = 0)\|} \tag{6}$$

Additionally, an amplitude amplification of a single vortex pair to the initial perturbation can be determined to only analyze the perturbation growth of that vortex pair. For the winglet tip vortices, which are the strongest vortices in all cases, this would give

$$A_{12} = \frac{\|(\eta_1, \zeta_1)_t\| + \|(\eta_2, \zeta_2)_t\|}{\|\Phi(t = 0)\|} \tag{7}$$

From the magnitude of the amplitude amplification A the degree of instability of the corresponding configuration can be judged. A further evaluation parameter is the ratio of amplitudes of the single vortices. Here a large ratio of wing-tip vortex to aileron vortex amplitude is preferable, because the wing-tip vortex is in most cases the strongest vortex in the wake of the model used here, thus responsible for the highest induced rolling moments. In the case of a 4-vortex system the ratio of wing-tip vortex to aileron vortex amplitude κ is defined as

$$\kappa = \frac{\sqrt{\eta_2^2 + \zeta_2^2}}{\sqrt{\eta_4^2 + \zeta_4^2}} \tag{8}$$

For a 6-vortex system, as shown in Fig. 10, two amplitude ratios κ_1 and κ_2 can be defined:

$$\kappa_1 = \frac{\sqrt{\eta_2^2 + \zeta_2^2}}{\sqrt{\eta_6^2 + \zeta_6^2}} \tag{9}$$

$$\kappa_2 = \frac{\sqrt{\eta_4^2 + \zeta_4^2}}{\sqrt{\eta_6^2 + \zeta_6^2}} \tag{10}$$

These specify the ratio of the wing-tip vortex and the bend vortex to the aileron vortex, respectively. Although these do not directly characterize the perturbation amplification of the vortices, they do give an indication as to which configurations are more likely to develop a strong cooperative instability. It has to be noted that in the frame of these stability analyses decay processes of the vortices due to viscosity or strong curvature of the vortex axis at high perturbation amplitudes are not covered. These effects are outside of the scope of the stability analysis. A low amplitude ratio now means that the aileron vortices theoretically get perturbed much faster than the stronger tip vortices. This means they will also disintegrate much faster in reality due to strong curvature, and thus prevent any further interaction. A configuration with a higher amplitude ratio now is more likely to exhibit a strong perturbation amplification of the tip vortices under the conditions of the real flow than those with a low amplitude ratio. So it is expected that configurations with a higher amplitude ratio κ will show a stronger effect on the vortex system in reality when actively excited with the winglet rudders.

IV. Flowfield Without Rudder Oscillation

A. Vorticity Distribution

Before the stability analyses, experimental investigations of the flowfield behind the model have been conducted to determine the parameters characterizing the vortex wake. Quantitative measurements with PIV have been supported by flowfield visualizations in the water towing tank. Several rudder/aileron combinations have been investigated at two different angles of attack without active oscillation of the winglet rudders. Configurations have been examined with presets of the winglet rudders of $\chi = 0$ deg,

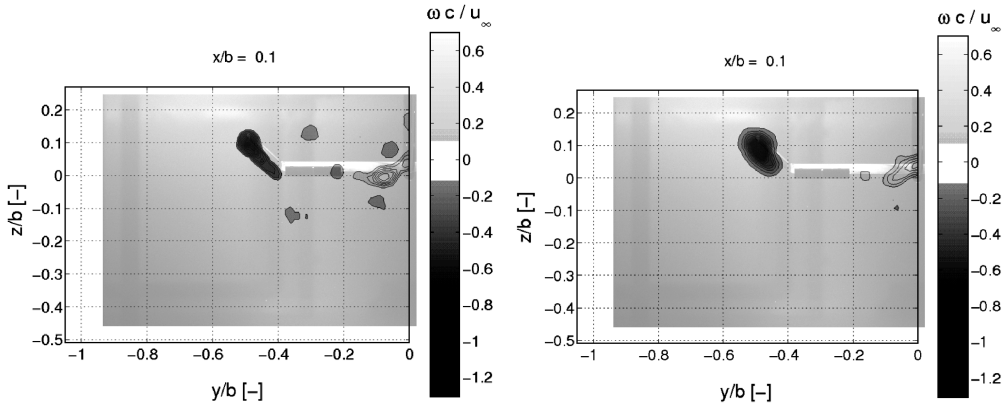

a) $\chi = 0$ deg, $\delta = 0$ deg **b) $\chi = +10$ deg, $\delta = 0$ deg**

Fig. 11 Vorticity distribution clean and with winglet rudder deflection, $\alpha = 11$ deg.

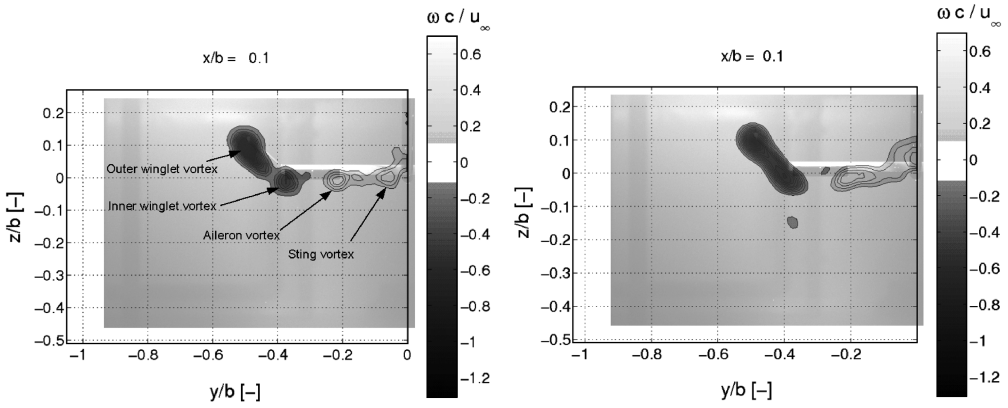

a) χ = +10 deg, δ = +20 deg **b) χ = 0 deg, δ = +20 deg**

Fig. 12 Vorticity distribution due to winglet rudder and aileron deflection, $\alpha = 11$ deg.

$+10$ deg, and -10 deg, presets of the ailerons of $\delta = 0$ deg and $+20$ deg at angles of attack of the wing of $\alpha = 4$ deg and 11 deg. These measurements give an insight into how the vortex system changes with different combinations of rudder deflection and yield the necessary input parameters for the subsequent stability analysis. Figure 11 first shows the vorticity distribution for the clean configuration without any rudder deflections, along with the vorticity distribution at a winglet rudder deflection of $\chi = +10$ deg. The vorticity is calculated from velocity data averaged over five individual measurements. The view is at the left half-plane from behind the model. It is noticeable that the winglet vortex is not only stronger due to the additional rudder deflection, but the vorticity is also more concentrated to the tip of the winglet.

Figures 12 and 13 show what happens when an additional aileron deflection is added. Three configurations, all with an aileron deflection of $\delta = 20$ deg at $\alpha = 11$ deg, but with a positive, a neutral, and a negative winglet rudder deflection are displayed. Clearly visible are the distinct vortices forming at the inner and outer aileron edges, as well as the winglet tip. Additionally a sting vortex can be seen, forming close to the centerline of the model at around $y/b = -0.1$. This vortex gets disrupted very quickly due to turbulent velocity components in the wake of the sting. But more important, it can be noted that the winglet rudder effectively shifts the center of vorticity on the winglet between the winglet tip and its base. A negative deflection shifts the resulting vortex inward, thus also influencing the span ratio of the stationary aileron vortex to the winglet vortex.

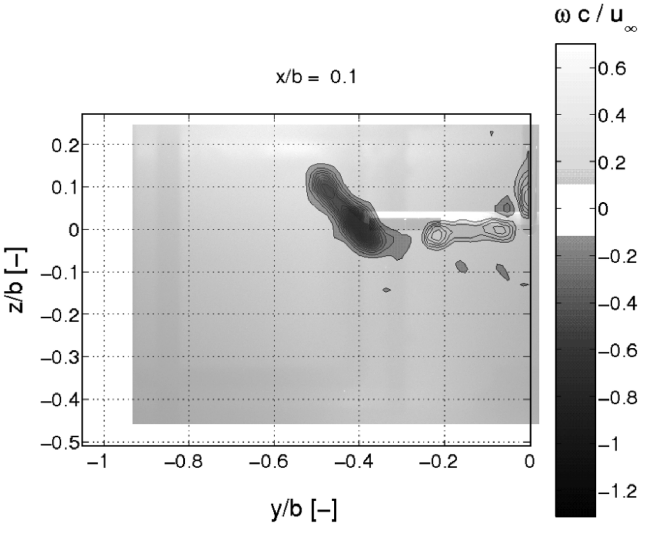

χ = -10 deg, δ = +20 deg

Fig. 13 Vorticity distribution due to winglet rudder and aileron deflection, $\alpha = 11$ deg.

The evolution of the flowfield of the configuration of Fig. 12a is shown in Fig. 14 for 12 stations behind the model. Note that these plots show flowfields of one individual measurement run. The inner and outer winglet vortices merge within the first few spans behind the model. It can be seen that the aileron vortex is still barely visible at $x/b = 11.7$ whereas beyond that only the merged inner and outer winglet vortex is still visible. The vortex core radius grows rapidly in the further evolution and the vorticity starts to spread over almost the whole observed plane. This already has a significant influence on the hazard level in the wake, which will be discussed further in the following section.

The corresponding vorticity distributions in the first plane for the positive and negative winglet rudder deflection at $\alpha = 4$ deg are shown in Fig. 15. The general influence of the winglet rudder is the same; however, at a negative rudder deflection the vorticity tends to concentrate even more near the bend between the winglet and the main wing. This is actually an example of a 4-vortex system as described in Sec. III. From these vorticity distributions the vortex parameters such as circulation and span ratios as well as the core radii of the vortices have been determined via a least-squares fit of a Lamb–Oseen vortex model at $x/b = 0.1$. Table 1 finally shows the parameters of the vortex systems of the investigated configurations.

B. Vortex Hazard

In addition to characterizing the vortex system by determining the vortex strengths and positions, a preliminary study of the wake vortex hazard to a following aircraft has been done by examining the induced rolling moments on a virtual following wing based on the measured velocity distributions. Figure 16a shows the evolution of induced rolling moments over distance behind the model for the clean model configuration, that is, without any rudder deflections, and for four different rudder configurations which all exhibit a counter-rotating aileron vortex pair. Plotted are the mean values of the maximum induced rolling moment cofficients of the five runs conducted per configuration, normalized by the lift coefficient C_L of the vortex-generating wing in the corresponding configuration. Typical standard deviation is around $\sigma = 0.05$ for a set of five measurements, so only the mean values will be compared here for more clarity. It can be seen that all values start at approximately the same level, but all the configurations with an additional aileron vortex pair seem to decay much faster, resulting in the induced rolling moment dropping considerably faster as well. The level of the induced rolling moment of the clean configuration at $x/b = 43$ is already reached at around 60% earlier in all four configurations.

This suggests that the presence of the additional aileron vortex causes this faster decay. Comparing the development of another configuration without aileron deflection, but only a winglet rudder deflection, shows that the induced rolling moment starts at a higher level (see Fig. 16b). The gradient $\Delta C_{\mathrm{RM}}/\Delta(x/b)$ however is about the same, although the induced rolling moment never drops significantly below that of the clean case. The higher initial rolling

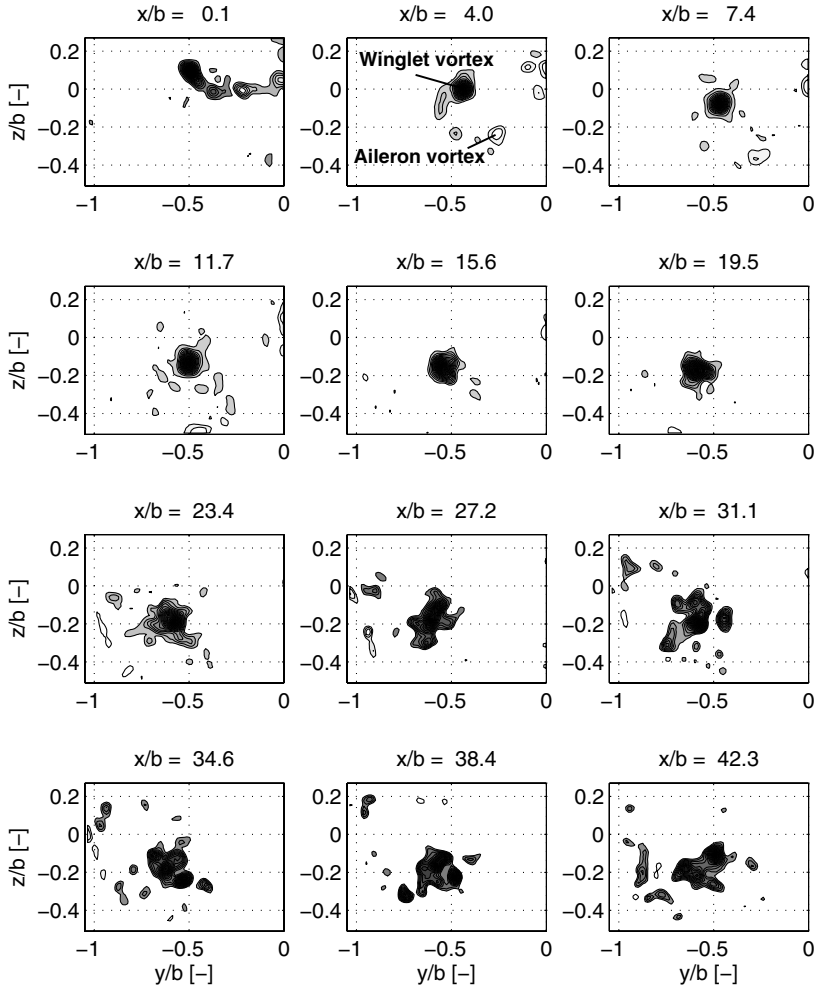

Fig. 14 Vorticity evolution with winglet rudder and aileron deflection, $\chi = +10$ deg, $\delta = +20$ deg, and $\alpha = 11$ deg.

moment is due to a higher concentration of vorticity, as shown in Fig. 11. The steeper gradient in the following suggests that there is another effect acting here as well that cannot be associated with the aileron vortex. This is most probably the self-induction of the tip vortex after it gets disturbed from a straight line by external influences, which eventually leads to a breakup of the vortex. This generally happens faster with a higher circulation in the vortex once it gets disturbed, thus leading to a faster rolling moment decay with the additional rudder deflection. The circulation contained in the winglet vortices Γ_{WL}, which is given in the figures as well, seems to support this explanation.

Finally, when comparing Fig. 16 to the corresponding vorticity distributions in Figs. 11–15, it can be stated that the spreading of vorticity over the span of the winglet obviously results in induced rolling moments shifted to lower levels. The steeper gradient in the development of the rolling moments, however, cannot clearly be attributed to the presence of an additional aileron vortex, but rather to the higher circulation contained in the vortices.

That the lower induced rolling moments indeed correspond to a faster decay of the vortex wake is supported by the vorticity distributions shown in Fig. 17. The vorticity of the configuration with rudder deflections in Fig. 17b is distributed over a much larger area than in the clean case, where a concentrated vortex core still persists.

This is also visible in the corresponding evolution of the circulation contained in the winglet vortices. Figure 18 shows the axial component of the circulation of the winglet vortices of the two

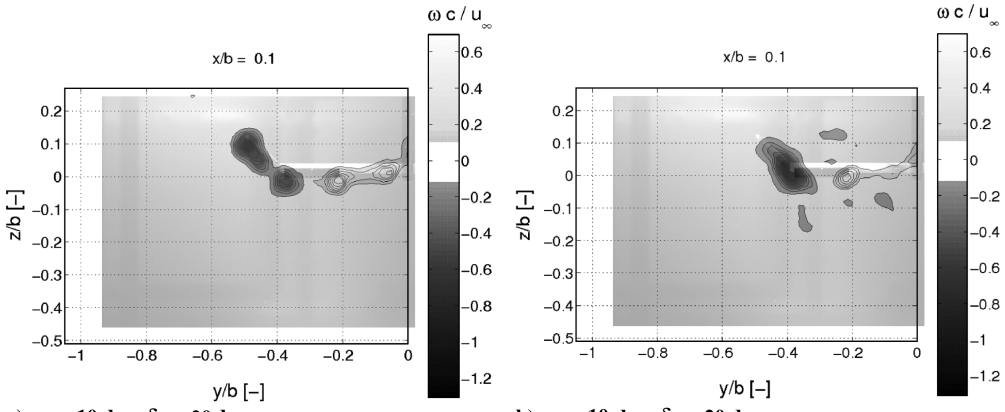

a) χ = +10 deg, δ = +20 deg **b) χ = -10 deg, δ = +20 deg**

Fig. 15 Shift of vorticity due to winglet rudder deflection, $\alpha = 4$ deg.

Table 1 Parameters of investigated configurations

2-vortex systems $\chi/\delta/\alpha$	b_2/b_1		Γ_4/Γ_2		$r_{c,2}[m]$	$r_{c,4}[m]$		C_L
0 deg /0 deg /11 deg	——		——		0.025	——		0.58
10 deg /0 deg /11 deg	——		——		0.026	——		0.62
4-vortex systems $\chi/\delta/\alpha$	b_2/b_1		Γ_4/Γ_2		$r_{c,2}[m]$	$r_{c,4}[m]$		C_L
−10 deg /10 deg /4 deg	0.49		−0.27		0.024	0.020		0.32
−10 deg /20 deg /4 deg	0.48		−0.38		0.026	0.024		0.41
6-vortex systems $\chi/\delta/\alpha$	b_3/b_1	b_2/b_1	Γ_6/Γ_2	Γ_4/Γ_2	$r_{c,2}[m]$	$r_{c,4}[m]$	$r_{c,6}[m]$	C_L
0 deg /20 deg /4 deg	0.40	0.80	−0.88	1.68	0.028	0.029	0.025	0.42
0 deg /20 deg /11 deg	0.38	0.81	−0.37	0.66	0.026	0.028	0.027	0.77
10 deg /20 deg /4 deg	0.41	0.76	−0.58	0.53	0.024	0.023	0.023	0.47
10 deg /20 deg /11 deg	0.40	0.75	−0.30	0.30	0.025	0.023	0.026	0.80
−10 deg /20 deg /11 deg	0.42	0.84	−0.75	2.69	0.024	0.027	0.026	0.76

above configurations over the complete measurement. Circulation has been calculated by integrating the measured vorticity distribution inside a circular region of $r = 4r_c$ around the winglet tip vortex while it descends. Here the vorticity of both vortices at the winglet tip and root is contained in the circulation (cf. Fig. 12a). As already observed, the circulation starts at a higher level when ailerons and winglet rudders are deflected. The circulation then decreases clearly faster and at the end nearly reaches the level of the clean configuration. Comparing this to Fig. 16 however, the larger spread of vorticity obviously results in noticeably lower induced rolling moments nevertheless.

C. Trajectory

In Fig. 19 eventually the trajectory of the configuration with rudder and aileron deflection is plotted in the measurement plane. The position of the model at $z/b = 0$ is also shown. The positions of the vortices are based upon the fitted Lamb–Oseen vortices, derived from the measured vorticity in each plane (see Sec. II). The descent of the vortices as well as a rotational motion is clearly visible. Note that the trajectory of the inner winglet vortex is only plotted up to a distance of $x/b = 6.5$, as it merges with the outer winglet vortex after that and is not recognizable as a single vortex anymore. The winglet and aileron vortex on the other hand remain separated over the whole measurement. The aileron vortex, however, leaves the observed measurement plane at about $x/b = 14$ and cannot be followed anymore.

D. Flow Visualization

A flow visualization using air bubbles has been done additionally to support the quantitative PIV measurements. The bubbles visualize the cores of the winglet tip vortex and make it possible to follow its path for a certain period. The example shown in Fig. 20 for two different stations downstream of the model with an aileron deflection of $\delta = 20$ deg proves that a sinusoidal instability on the vortices takes place, which is not as apparent in the clean case shown in Fig. 21 at the same positions. Note that the aileron vortex is not

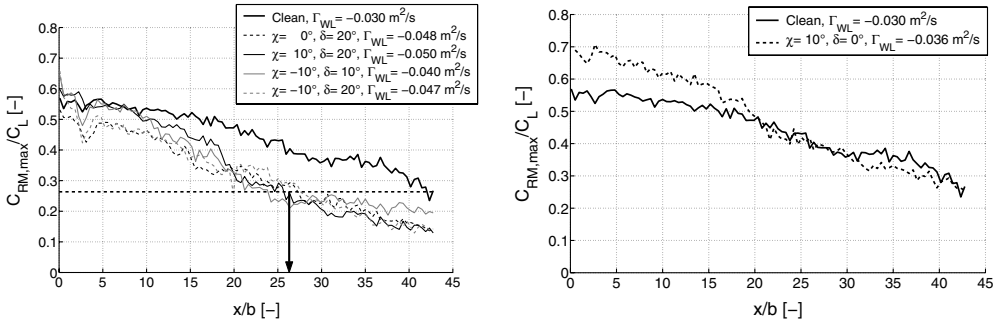

a) With aileron vortex **b) Without aileron vortex**

Fig. 16 Maximum induced rolling moment coefficient, $\alpha = 11$ deg, $b_F = 0.2b$.

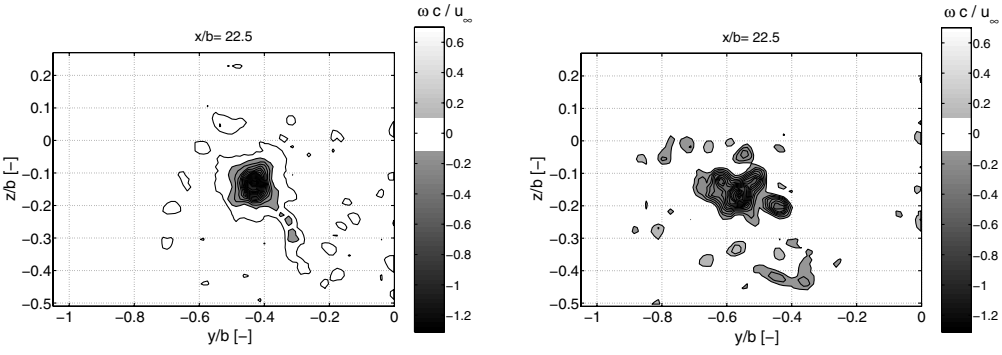

a) Clean **b) χ = +10 deg, δ = +20 deg, α = 11 deg**

Fig. 17 Vorticity distributions at $x/b = 22.5$.

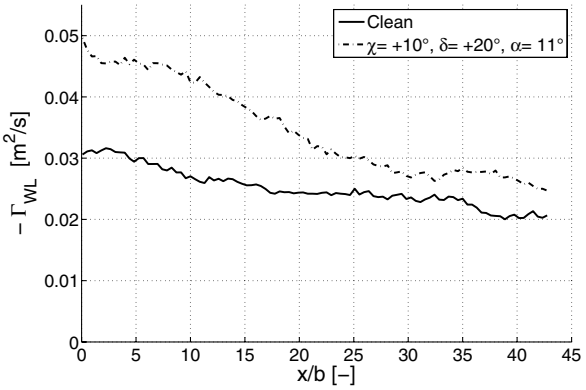

Fig. 18 Evolution of circulation in winglet vortices.

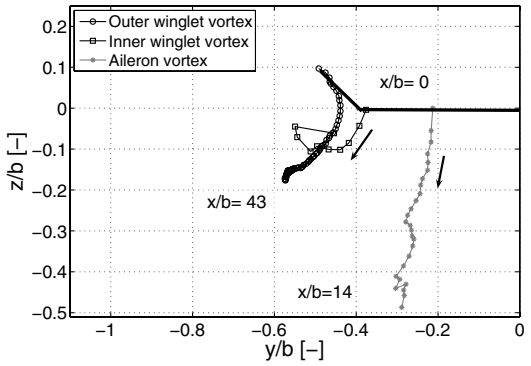

Fig. 19 Trajectory of winglet and aileron vortices in the *y*–*z* plane, $\chi = +10$ deg, $\delta = +20$ deg, and $\alpha = 11$ deg.

visible here because a bubble injection close to the aileron edge is lacking.

The wavelength of the sinusoidal perturbation visible in Fig. 20 can be determined from the pictures to be roughly $\lambda = 0.5$ m$\pm$ 10%, which is in good agreement with the numerical results of the stability analysis shown later.

V. Theoretical Results

After determining the necessary vortex system parameters from the initial PIV measurements numerical calculations could be carried out to analyze the stability of the different vortex systems and to determine the frequencies for a subsequent active excitation with the winglet rudders. Based on the values shown in Table 1, the calculations have been conducted according to the description given in Sec. III, and the corresponding evaluation parameters could be derived. A typical result of a stability analysis of a 4-vortex system, in this case of a configuration with $\chi = -10$ deg and $\delta = +20$ deg at $\alpha = 4$ deg angle of attack, is shown in Fig. 22a. It shows that an extended peak develops at high wave numbers of around $kb_0 = 12$, corresponding to an oscillation frequency of the rudders of $f = 2.8$ Hz. Comparison with the peak of the Crow instability seen in the lower left corner makes clear the large potential of those instabilities. The plot also shows that a small deviation from the theoretical optimum wave number, due to uncertainties in the input data to the calculations, for example, does not significantly lower the theoretical growth rate of the developing instability.

Figure 22b shows the corresponding eigenvectors of the most unstable eigenmode of this configuration at a wave number of $kb_0 = 12$, with the perturbation amplitudes of the single vortices according to Fig. 9. The inner aileron vortices are perturbed much stronger than the wing-tip vortices, obviously due to their lower circulation. This is a characteristic of all the investigated configurations, and could lead to an earlier destruction of the aileron vortices in the real flow because of higher curvature of the vortices at a given wave number. This early destruction of the second vortex pair would lower the efficiency of the cooperative instabilities between the vortices.

In Fig. 23 the amplitude amplification for a typical 6-vortex configuration plotted over the wave number of the excitation is shown (compare also Fig. 12b). An initial perturbation amplitude of a magnitude of

$$\|\Phi(t=0)\| = 10^{-4} b_0 \tag{11}$$

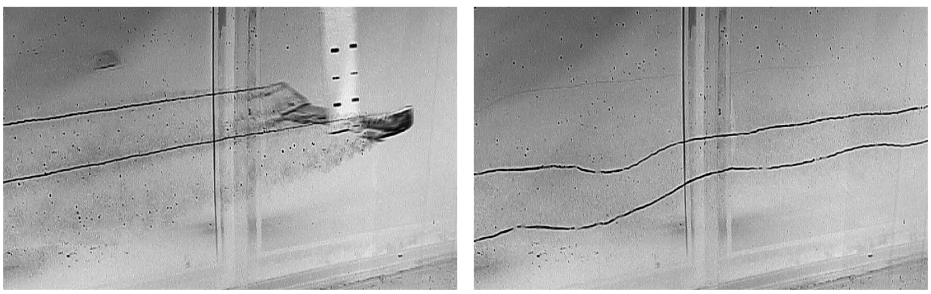

a) *x/b* = 0 **b) *x/b* = 7**

Fig. 20 Flow visualization of winglet vortex with $\chi = 0$ deg and $\delta = +20$ deg aileron deflection, $\alpha = 11$ deg.

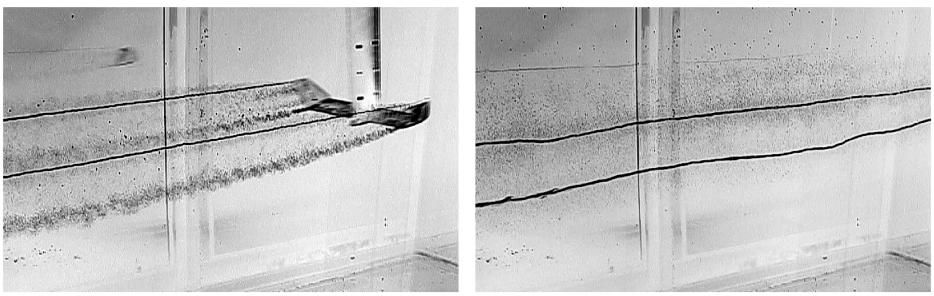

a) *x/b* = 0 **b) *x/b* = 7**

Fig. 21 Flow visualization of winglet vortex, clean, $\alpha = 11$ deg.

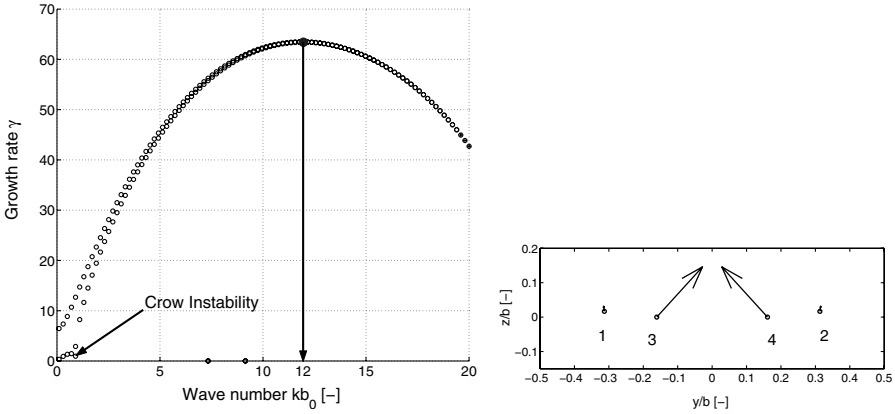

a) Resulting growth rates **b) Eigenvectors of most unstable eigenform at $kb_o = 12$**

Fig. 22 Result of stability analysis, $\chi = -10$ deg, $\delta = +20$ deg, and $\alpha = 4$ deg.

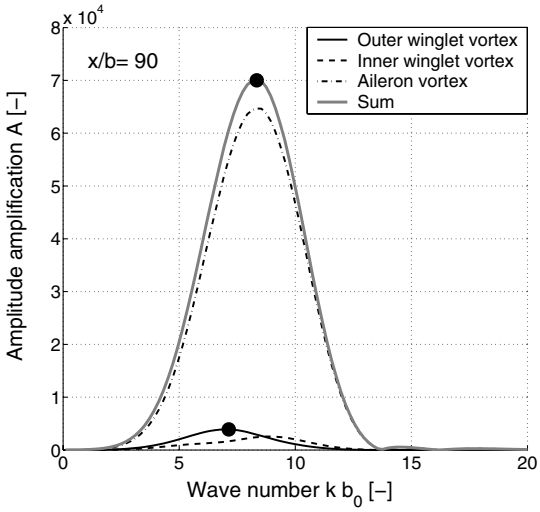

Fig. 23 Amplitude amplification for a 6-vortex configuration $\chi = 0$ deg, $\delta = +20$ deg, and $\alpha = 11$ deg.

has been imposed upon the vortices. The perturbation amplitudes of the single vortex pairs at $x/b = 90$ spans behind the model related to this initial amplitude are displayed. Again, it can be noted that the weaker aileron vortices become perturbed much stronger than the stronger vortices on the winglet. The maxima of amplification lie very close to each other, yet at slightly different wave numbers. Experiments with two different wave numbers have been conducted, that of maximum amplification of the outer winglet vortex, being the strongest vortex responsible for the maximum induced rolling moment, and that of maximum amplification of the sum of the perturbation amplitudes of all vortices. Both are marked by dots in Fig. 23.

Figure 24 shows the actual perturbations of the vortices at $x/b = 90$ for the wave number corresponding to the strongest perturbation of the outer winglet vortex along with the initially imposed perturbation scaled to the same total length and at the same vortex positions as at the wing's trailing edge. The actual positions of the vortices are different because of their descending and rotating motion. The plot, however, demonstrates the relative magnitudes and orientations of the perturbations of the different vortices. The amplitude ratio of the perturbations of the two winglet vortices to those of the aileron vortex are $\kappa_1 = 0.07$ and $\kappa_2 = 0.12$.

Table 2 contains all results for the wave numbers leading to maximum instability and their corresponding wavelengths. Additionally, the amplitude ratios κ_i of the outer vortices to the aileron vortex are given. It can be seen that the amplitude ratios are

Table 2 Wave numbers and wavelengths for maximum instability and amplitude ratios

4-vortex systems				
$\chi/\delta/\alpha$	kb_0	$\lambda[m]$	κ	
−10 deg /10 deg /4 deg	12.6	0.307	0.038	
−10 deg /20 deg /4 deg	12.0	0.419	0.080	
$\chi/\delta/\alpha$	kb_0	$\lambda[m]$	κ_1	κ_2
6-vortex systems (whole system)				
0 deg /20 deg /4 deg	10.6	0.475	0.244	0.125
0 deg /20 deg /11 deg	8.3	0.452	0.055	0.109
10 deg /20 deg /4 deg	5.9	0.895	0.170	0.633
10 deg /20 deg /11 deg	9.9	0.400	0.024	0.040
−10 deg /20 deg /11 deg	12.2	0.300	0.030	0.032
6-vortex systems (strongest vortex)				
0 deg /20 deg /4 deg	9.5	0.525	0.232	0.134
0 deg /20 deg /11 deg	7.1	0.528	0.066	0.120
10 deg /20 deg /4 deg	4.1	1.288	0.215	0.319
10 deg /20 deg /11 deg	7.3	0.543	0.068	0.208
−10 deg /20 deg /11 deg	9.7	0.373	0.066	0.060

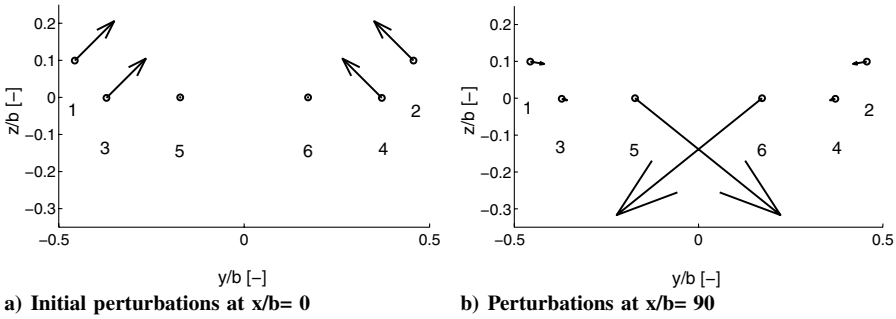

a) Initial perturbations at x/b= 0 **b) Perturbations at x/b= 90**

Fig. 24 Perturbations of single vortices, $\chi = 0$ deg, $\delta = +20$ deg, and $\alpha = 11$ deg (not to scale).

consistently smaller than 1, corresponding to the fact that the aileron vortex is always perturbed much stronger than the outer vortices, as demonstrated in Figs. 22–24. It is also noticeable that higher amplitude ratios develop only with lower angles of attack because the strength of the aileron vortex relative to the outer vortices is generally higher in these cases. In configurations with a high angle of attack and additional aileron deflection, which come close to a landing configuration, the amplitude ratio is quite low throughout.

VI. Experimental Results with Rudder Oscillation

In this section some experimental results of the measurements with active winglet rudder oscillation will be presented. The wave numbers obtained during the stability analysis and shown in Table 2 have been generated by means of a periodic motion of the winglet rudders while towing the model through the tank. That way the inherent instabilities in the vortex system should be excited and their initiation accelerated. Two different oscillation amplitudes have been employed for the winglet rudders. A smaller amplitude would be preferable to minimize lift variation during the oscillation, as there is no means of compensating those variations on the present model. However, to make sure the effect is not prevented due to an amplitude which is too small, a higher amplitude has additionally been chosen. Thus, rudder oscillation amplitudes of ± 5 deg and ± 10 deg have been employed and compared.

A. Induced Rolling Moments

Figure 25 shows a result for the configuration with $\delta = 20$ deg aileron deflection and clean winglet rudders. Despite the high scatter between the individual measurements the mean values will be considered in the following figures as well. Some individual runs show a somewhat more unsteady development although this is not reproducible. To show the order of magnitude of the scatter the five individually measured evolutions of the induced rolling moments are plotted additionally in Figs. 25a and 25c. The standard deviation in this example ranges up to a maximum of $\sigma = 0.06$.

Figure 25a contains the induced rolling moment coefficients for the five single measurement runs in comparison to the static case for one of the wave numbers in Table 2. It is apparent that the values of the induced rolling moments are not significantly below the values with static rudders. Oscillation with a different wave number, corresponding to maximum theoretical amplification of the whole vortex system, gives the same result qualitatively, as shown in Fig. 25b. Both mean values do not drop significantly below the static values.

Figure 25c shows that even the higher oscillation amplitude does not result in a viable alleviation of the wake hazard. Developments of the induced rolling moments show a somewhat higher scatter between single measurements, but their values average to be only slightly below the static case up to about 25 spans. The final level does not sink below and is not expected to do so in the further development of the wake. The same behavior is observed with all the other configurations examined. Therefore, the attempt to further alleviate the wake vortex hazard by actively exciting the periodic instabilities in the wake with the help of an additional winglet rudder oscillation has to be considered unsuccessful.

A possible explanation for this behavior shall be given nevertheless. As the experimental results in Sec. IV suggest, some degree of instability obviously already exists, even with static rudders. The initial perturbation needed to initiate these instabilities must be induced by external effects caused by the mounting of the model in the tank, the residual velocities in the water, or an influence of the tank itself. Hence, an additional active excitation of the vortices does not cause the instabilities to become active much earlier, and the vortex decay develops the same, as shown by means of the induced rolling moments. The frequency range of these external perturbations, however, is not known. Their determination would require measurements with a higher spatial and temporal resolution.

B. Flow Visualization

For another configuration flow visualization snapshots with rudder oscillation are shown in Fig. 26. It is obvious that the periodic perturbations with the wavelength of the rudder oscillation actually get superimposed on the vortices. The oscillation wave number corresponds to a wavelength of $\lambda = 0.4$ m in this case. However, the

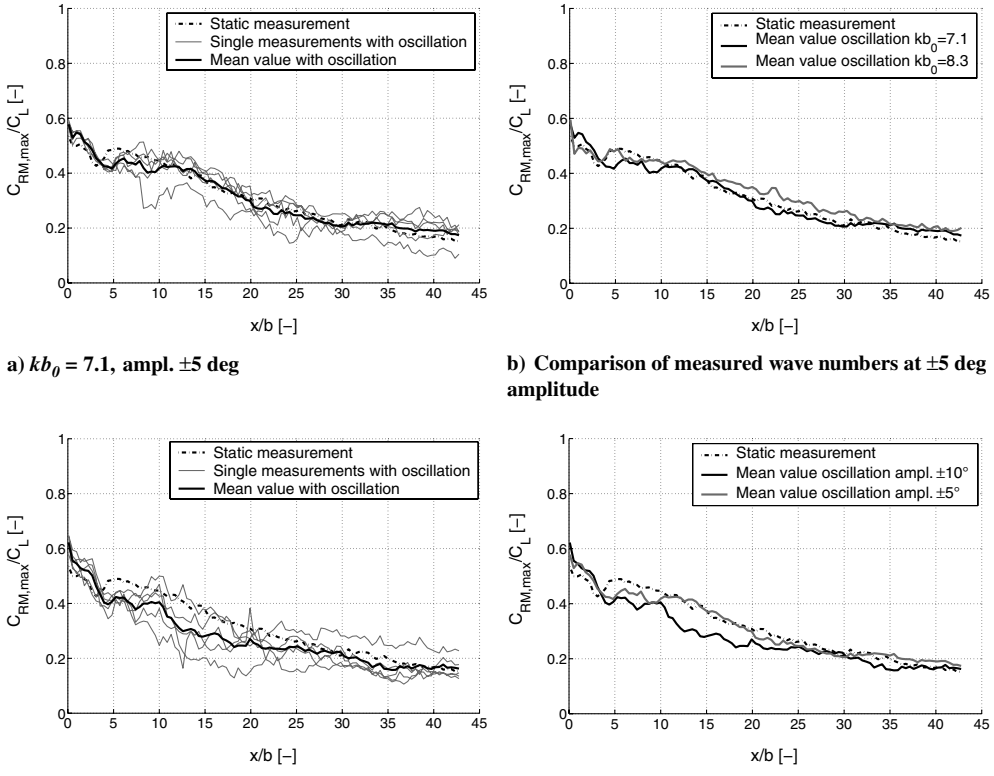

a) $kb_0 = 7.1$, ampl. ±5 deg

b) Comparison of measured wave numbers at ±5 deg amplitude

c) $kb_0 = 7.1$, ampl. ±10 deg

d) Comparison of measured amplitudes at $kb_0 = 7.1$

Fig. 25 Results of measurements with oscillating winglet rudder, $\chi = 0$ deg, $\delta = +20$ deg, and $\alpha = 11$ deg.

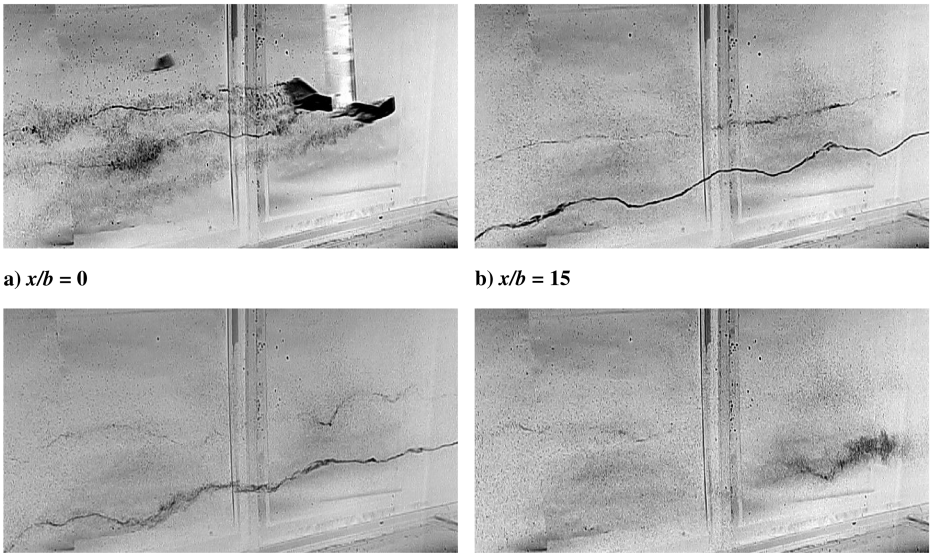

a) $x/b = 0$ b) $x/b = 15$

c) $x/b = 19$ d) $x/b = 29$

Fig. 26 Flow visualization with oscillating winglet rudder, $\chi = +10$ deg, $\delta = +20$ deg, and $\alpha = 11$ deg, oscillation amplitude ± 10 deg, $kb_0 = 9.9$.

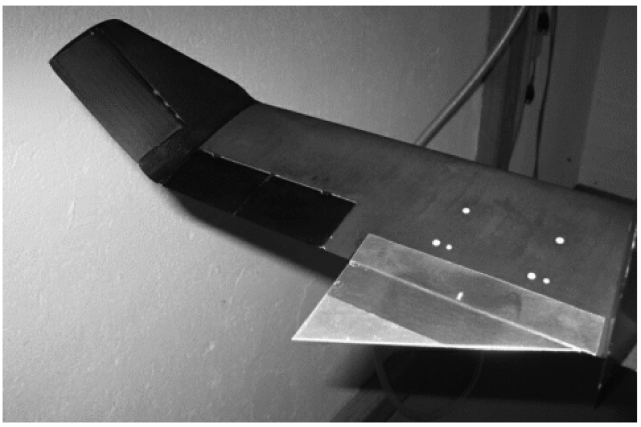

Fig. 27 Inboard flaps on model.

sinusoidal perturbations do not grow rapidly as is expected. In fact, the vortices remain relatively stable up to a distance of about 19 spans to the model. After 29 spans the air bubbles finally dissipate from the vortex cores, showing the advanced aging of the vortices. This behavior supports the conclusion drawn from the induced rolling moment development before. The winglet rudder oscillation does not seem to help destabilize the vortex system behind the wing.

VII. Experimental Results with Additional Flaps

Additional measurements with triangular flaps attached to the model have been conducted as well to be able to further vary the parameters of the resulting vortex system. The flaps are uncambered and have been fitted to the underside of the wing's profile at an angle of incidence of 8 deg to the wing chord. They form a pair of inboard flaps producing a vortex pair corotating with the winglet tip vortex; see Fig. 27. They have additionally been moved to different spanwise positions to determine the influence of a variation of the span ratio of the emerging vortices. Span ratios of flap to winglet vortex between $b_{\text{flap}}/b_{\text{winglet}} = 0.41$ and 0.81 have been examined. The circulation ratio between the flap and the winglet vortex is $\Gamma_{\text{flap}}/\Gamma_{\text{winglet}} = 0.54$ for all flap span ratios, resulting in a constant lift coefficient of $C_L = 0.72$. Results show that the spanwise position of the flaps has a significant influence on the decay of the vortex wake, causing an early breakdown of the vortex system if the flap vortex is close enough to the winglet vortex. During the course of the experiments it has also been noticed that a small sideslip angle of about $\beta = 1$ deg noticeably enhances breakdown of the vortex system if the winglet is on the lee side of the incoming flow.

Figure 28a shows the corresponding induced rolling moments for the innermost flap position with $b_{\text{flap}}/b_{\text{winglet}} = 0.41$, which was chosen as the reference case because it is the most stable configuration. The induced rolling moment evolutions have been averaged over five individual measurement runs for each configuration. Additionally the most unstable configuration at $b_{\text{flap}}/b_{\text{winglet}} = 0.68$ is shown as measured with a symmetrical inflow as well as a sideslip of the model to both sides. It is obvious that with an additional sideslip angle to the right direction, clarified in Fig. 28b, the early breakdown of the vortex system takes place much more efficiently than without sideslip, or even a sideslip in the opposite direction. The winglet being on the lee side corresponds to a small spanwise component of the incoming flow (cf. Fig. 28b). Possibly

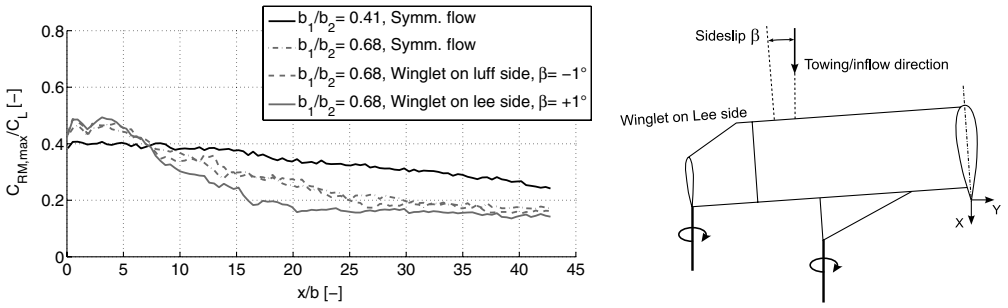

a) Influence of sideslip angle b) Definition of sideslip

Fig. 28 Induced rolling moments with inboard flaps, clean, $\alpha = 11$ deg.

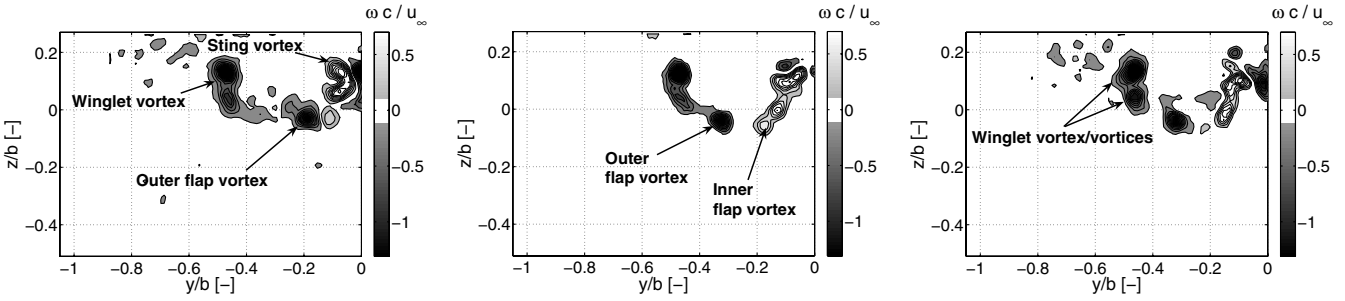

a) $b_{flap}/b_{winglet}$ **= 0.41** **b)** $b_{flap}/b_{winglet}$ **= 0.68, symmetrical flow** **c)** $b_{flap}/b_{winglet}$ **= 0.68, winglet on lee side**

Fig. 29 Vorticity distribution with outboard flaps at $x/b = 0.5$, $\alpha = 11$ **deg.**

aided by the dihedral of the winglet, this could be a beneficial factor for the breakdown of the vortex forming there. On the other hand, the sting mount which is moved into sideslip along with the wing might have an influence as well. Comparative measurements with a straight wing tip resulting in the same aspect ratio of the wing, which are not shown in detail here, have yielded no definite influence of sideslip, however. This supports the statement that the effect is due to the flow around the winglet tip resulting from the dihedral. The effect still needs further investigation, however.

In Fig. 29 the instantaneous vorticity distribution for three of the cases is displayed directly behind the trailing edge. Shown from left to right are the stable reference case, the most unstable flap position in symmetrical flow, and the most unstable flap position with a favorable sideslip. The general formation of the vortex system into mainly two corotating vortex pairs is visible. With the outer flap positions in Figs. 29b and 29c, a distinct inner, counter-rotating flap vortex develops as well, which otherwise gets mixed up with the sting vortex when the flap is located too close to the sting, Fig. 29a. Also, a tendency of the vorticity behind the winglet to evolve into two distinct vortices is visible with the positive sideslip in Fig. 29c.

Figure 30 shows how the wake evolved after $x/b = 7.4$. Whereas for the inner flap position in Fig. 30a the two corotating vortices are clearly visible, the two plots for the outer flap position show the corotating outer as well as the counter-rotating inner flap vortex rotating around the winglet vortex. For the inner flap position, the inner aileron vortex has been entrained into the quickly dissolving sting vortex.

Figure 31 now displays the flowfield at an even later stage in the wake at $x/b = 16.5$. It can be seen that the vorticity is still concentrated in mainly one vortex in the first two cases. But when a sideslip angle is employed (Fig. 31c) the vorticity at the same downstream distance is already spread over almost the whole measurement field and no concentrated vortex core is discernible anymore. This supports the results from the induced rolling moment evolutions shown before.

The vorticity patches outside the vortex cores, visible especially in greater distance to the wing, are obviously caused by exchange of vorticity with the surrounding flow. Their distribution is not reproducible across measurements and thus appear more noticeable in the instantaneous flowfields, while they are less visible in the averaged vorticity distributions as in Figs. 11–15, for example.

Finally, Fig. 32 contains two criteria which are used to judge the effect of flap position on the breakdown of the vortex system. The configuration with the innermost flap position is chosen as the reference case, as mentioned before. Figure 32a shows the remaining induced rolling moment level at the end of the measurement at

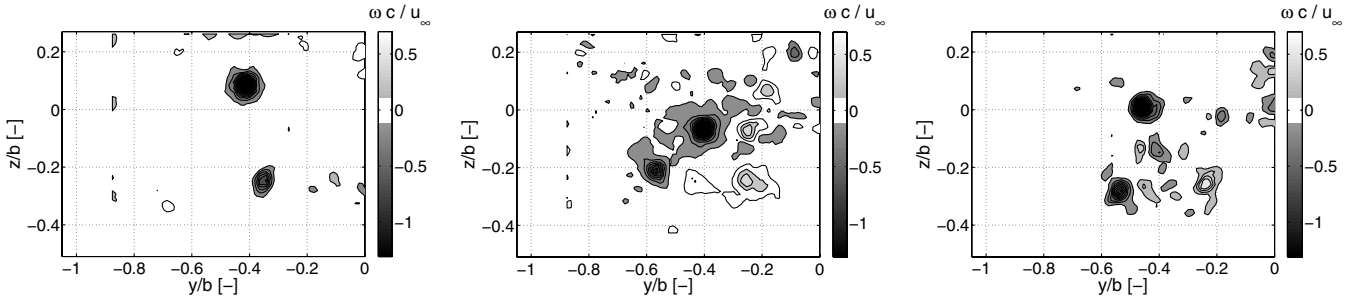

a) $b_{flap}/b_{winglet}$ **= 0.41** **b)** $b_{flap}/b_{winglet}$ **= 0.68, symmetrical flow** **c)** $b_{flap}/b_{winglet}$ **= 0.68, winglet on lee side**

Fig. 30 Vorticity distribution with outboard flaps at $x/b = 7.4$, $\alpha = 11$ **deg.**

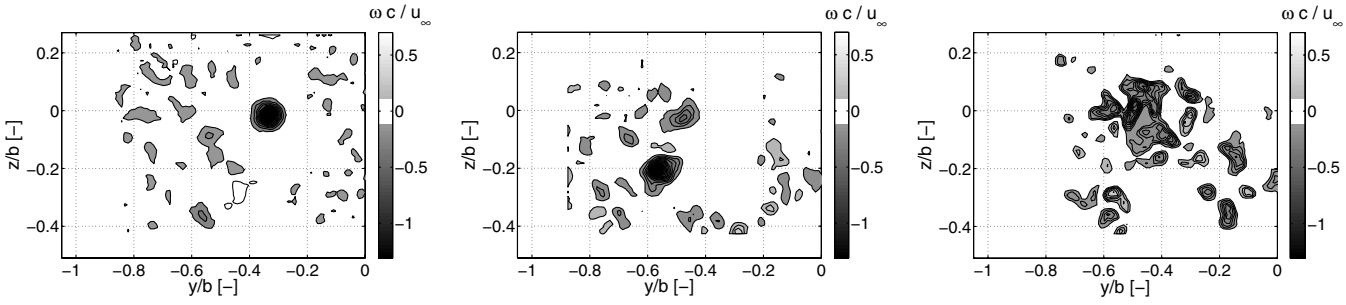

a) $b_{flap}/b_{winglet}$ **= 0.41** **b)** $b_{flap}/b_{winglet}$ **= 0.68, symmetrical flow** **c)** $b_{flap}/b_{winglet}$ **= 0.68, winglet on lee side**

Fig. 31 Vorticity distribution with outboard flaps at $x/b = 16.5$, $\alpha = 11$ **deg.**

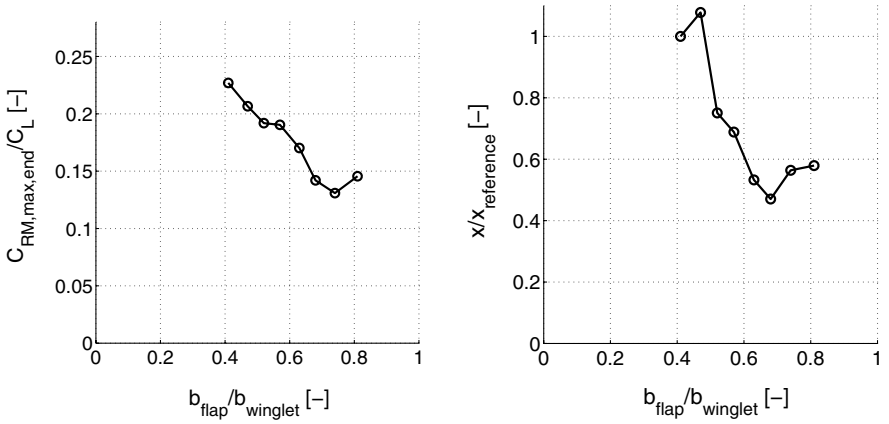

a) Final level of induced rolling moment **b)Position of reaching final level of reference conf.**

Fig. 32 Effect of span ratio between flap and winglet vortex.

$x/b = 43$ for the different span ratios used. The final rolling moment level of the reference case is taken as a reference level. Figure 32b now shows the relative position at which this reference level is reached depending on the span ratio. It is apparent that besides a significant reduction of the rolling moment level in the farfield a corresponding level of an unaffected, stable configuration can be reached much earlier. In the experiments presented here it was possible to reduce the distance to reach the reference rolling moment to about 50%. As the induced rolling moment does not increase anymore after that, this would allow a reduction in the separation distance between two consecutive aircraft by the same ratio if the reference rolling moment level is defined as a safe level. The optimum span ratio for both of the criteria is around $b_{\text{flap}}/b_{\text{winglet}} = 0.7$.

The interaction between the vortex pairs seems to be very effective despite the fact that theoretically the growth rates of the instabilities of corotating vortex pairs are an order of magnitude smaller than with counter-rotating vortex pairs. One reason for the growing effectiveness of the instabilities may therefore be the additional counter-rotating vortex pair which forms when the flaps are moved far enough outward. It is known that counter-rotating vortex pairs exhibit much stronger instabilities than corotating ones. Figure 33 shows the results of a stability analysis of the most unstable flap position at $b_{\text{flap}}/b_{\text{winglet}} = 0.68$, containing all three vortex pairs that emerge behind the winglet and flap. The corresponding parameters of the vortex system are given as follows: $b_3/b_1 = 0.34$; $b_2/b_1 = 0.68$; $\Gamma_6/\Gamma_2 = -0.54$; $\Gamma_4/\Gamma_2 = 0.53$; $r_{c,2} = 0.021m$; $r_{c,4} = 0.018m$; $r_{c,6} = 0.023m$; $C_L = 0.76$. It is obvious that the amplitude amplification A is orders of magnitude lower than in the similar case presented in Fig. 23. The difference here is that the single vortices are separated further from each other than in the case with only the integrated ailerons deflected (cf. Fig. 12). Still, the experiments show that in reality the instabilities are not prevented from occurring. This may be due to the influence of the third, counter-rotating vortex pair from the inner flap edges. There is an obvious discrepancy between theory and experiments visible here, which has to be accounted to the strong nonlinear processes occurring in the vortex system in its most unstable configuration.

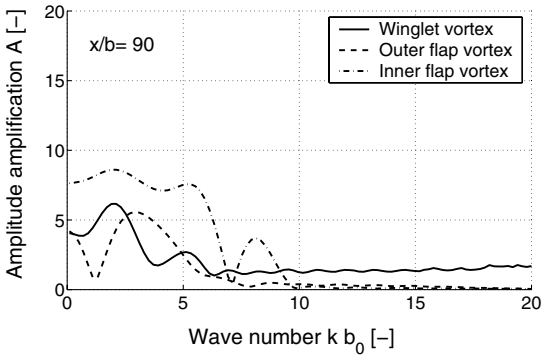

Fig. 33 Result of stability analysis for most unstable flap position, $b_{\text{flap}}/b_{\text{winglet}} = 0.68$.

VIII. Conclusion

Experimental investigations have been conducted in this work to examine if winglets can be employed to alleviate the wake vortex hazard emanating from that wing. To that purpose rudders, which could be oscillated as well as deflected statically, have been integrated into the winglets. Results of the measurements showed that an oscillation with the theoretically optimum wave number does not further accelerate the decay of the hazard level in the wake. However, extensive experiments with statical rudders and additional flap extensions on the model have shown that it is possible to destabilize the vortex system faster, even without active measures, with the right choice of configuration parameters. An outboard flap at the right spanwise position enhances an early breakdown of the vortices. Configurations without an actual deflection of the winglet rudders have proven here to be almost as effective as those with rudder deflection. So for the exploitation of wake vortex instabilities the active rudders are obviously not necessary. Whether or not this mechanism is as effective under real flight conditions still has to be investigated, however. Span ratios between the outer flap edge and wing tip of common transport aircraft wings are already in the region that has been found to be the optimum in this work, which questions the additional use of this approach. However, the ratio of core radii to vortex separation distances in one half-plane are on the order of $r_c/d = 0.2$–0.3 in the presented experiments, which is quite large in comparison to flight conditions, mainly due to the higher core radii. This ratio has an influence on the development of the emerging instabilities as well, which makes increasing this ratio a promising approach, as suggested already by Laporte [17]. This would have to be achieved either by enlarging the vortex core radii sufficiently or by varying the flap span and thus bringing the flap and wing-tip vortex closer together. A winglet equipped with some kind of rudder could be useful again here, as it can be used to shift the wing-tip vortex position to a certain extent.

Furthermore, a sensitivity of the vortex wake to a small sideslip of the wing model has been noticed during the experiments. This suggests that the stability of the vortices forming at the winglet are influenced by the dihedral of the winglet. If the sideslip is really the reason for an accelerated breakdown, an arrangement of the winglets in the right manner during landing approach could be used to support wake vortex breakdown behind the aircraft. A sweep of the wing could be exploited to establish a flow condition on the winglet similar to that in the experiments shown here. A flight in sideslip, however, would be unfavorable due to the fact that only one wing would have the optimum inflow direction as determined in Sec. VII. This effect

should be investigated in more detail in the future. Also, a possible influence of the sting mount must be ruled out.

Acknowledgment

This work was funded by the German government within the framework of the Luftfahrtforschungsprogramm 3.

References

[1] Crouch, J. D., Miller, G. D., and Spalart, P. R., "An Active-Control System for Breakup of Airplane Trailing Vortices," *AIAA Journal*, Vol. 39, No. 12, 2001, pp. 2374–2381.

[2] Ortega, J. M., Bristol, R., and Savaş, O., "Wake Alleviation Properties of Triangular-Flapped Wings," *AIAA Journal*, Vol. 40, No. 4, 2002, pp. 709–721.

[3] Stuff, R., "Alleviation of Aircraft Vortex Hazard Through Passive Aerodynamic Measures," AIAA Paper 2003-1108, 2003.

[4] Vollmers, H., Bao, F., Castagno, F., and Mattner, H., "Measurement on the Interaction and Stability of Four Vortex Wakes," EuroMech Kolloquium No. 433, März 2002, Aachen.

[5] Haverkamp, S., Neuwerth, G., and Jacob, D., "Active and Passive Wake Vortex Mitigation Using Control Surfaces," *Aerospace Science and Technology*, Vol. 9, No. 1, 2005, pp. 5–18.

[6] Durston, D. A., Walker, S. M., Driver, D. M., and Smith, S. C., "Wake-Vortex Alleviation Flowfield Studies," *Journal of Aircraft*, Vol. 42, No. 4, 2005, pp. 894–907.

[7] ECCOMAS, *Status of Onera Research on Wake Vortex in the Framework of National Activities and European Collaboration*, 2004.

[8] Park, P. S., and Rokhsaz, K., "Effects of a Winglet Rudder on Lift-to-Drag Ratio and Wake Vortex Frequency," AIAA Paper 2003-4069, 2003.

[9] Crow, S. C., "Stability Theory for a Pair of Trailing Vortices," *AIAA Journal*, Vol. 8, No. 12, 1970, pp. 2172–2179.

[10] Crouch, J. D., "Instability and Transient Growth for Two Trailing-Vortex Pairs," *Journal of Fluid Mechanics*, Vol. 350, Nov. 1997, pp. 311–330.

[11] Fabre, D., and Jacquin, L., "Stability of a Four-Vortex Aircraft Wake," *Physics of Fluids*, Vol. 12, No. 10, 2000, pp. 2438–2443.

[12] Fabre, D., Jacquin, L., and Loof, A., "Optimal Perturbations in a Four-Vortex Aircraft Wake in Counter-Rotating Configuration," *Journal of Fluid Mechanics*, Vol. 451, Jan. 2002, pp. 319–328.

[13] Gerz, T., Holzäpfel, F., and Darracq, D., "Commercial Aircraft Wake Vortices," *Progress in Aerospace Sciences*, Vol. 38, No. 3, 2002, pp. 181–208.

[14] Neuwerth, G., "Strömungssichtbarmachung in Wasserkanälen Mittels eines Verfahrens zur Erzeugung Feinster Luftbläschen," *Zeitschrift fur Flugwissenschaften und Weltraumforschung*, Vol. 9, No. 3, 1985, pp. 187–189.

[15] Bao, F., and Vollmers, H., "Alleviation of End-Effect in Facilities for Far Wake Investigations," AIAA Paper 2005-0907, 2005.

[16] Nayfeh, A. H., and Mook, D. T., *Nonlinear Oscillations*, Wiley, New York, 1979, Chap. 5.2.

[17] Laporte, F., and Leweke, T., "Elliptic Instability of Counter-Rotating Vortices: Experiment and Direct Numerical Simulation," *AIAA Journal*, Vol. 40, No. 12, 2002, pp. 2483–2494.

F. Coton
Associate Editor